Applied Surface Science 440 (2018) 1027–1036

Contents lists available at ScienceDirect

Applied Surface Science

journal homepage: www.elsevier.com/locate/apsusc

Full Length Article

Enhancing pseudocapacitive kinetics of nanostructured MnO_2 through anchoring onto biomass-derived porous carbon

Qiongyu Chen [a], Jizhang Chen [a,*], Yuyang Zhou [a], Chao Song [a], Qinghua Tian [b], Junling Xu [c], Ching-Ping Wong [c]

[a] College of Materials Science and Engineering, Nanjing Forestry University, Nanjing 210037, China
[b] Department of Chemistry, School of Sciences, Zhejiang Sci-Tech University, Hangzhou 310018, China
[c] Department of Electronic Engineering, The Chinese University of Hong Kong, New Territories, Hong Kong

ARTICLE INFO

Article history:
Received 9 November 2017
Revised 16 January 2018
Accepted 25 January 2018
Available online 31 January 2018

Keywords:
Manganese dioxide
Biomass
Porous carbon
Heterostructure
Supercapacitors

ABSTRACT

The rational construction of heterostructured electrode materials that deliver superior performances to their individual counterparts offers an attractive strategy for supercapacitors. Herein, we anchor low-crystalline nanostructured MnO_2 onto soybean stalk-derived carbon matrix through chemical activation and subsequent hydrothermal reaction. The highly porous and conductive matrix can effectively enhance pseudocapacitive kinetics of nanostructured MnO_2. Therefore, the obtained nanocomposite exhibits high specific capacitance (384.9 F g^{-1} at a current density of 0.5 A g^{-1}), great rate capability (185.0 F g^{-1} at 20 A g^{-1}), and superior cyclability (90.7% capacitance retention after 5000 cycles). Using this nanocomposite as the positive electrode material, an asymmetric supercapacitor (ASC) is assembled, and achieves high specific energy of 34.2 Wh kg^{-1} and high specific power of 9.58 kW kg^{-1}. The results of this study demonstrate great potential of combining biomass-derived porous carbon with metal oxides.

1. Introduction

Efficient, reliable, and cost-effective electrochemical energy storage (EES) devices are highly desired to meet the ever-increasing requirements for charge storage [1]. Among various emerging EES devices, supercapacitors are attractive for a wide range of applications, such as energy recovery systems, backup power systems, smart grids, and high-rate power sources (*e.g.*, mobile laser weapons and mining shovels), owing to their high specific power, good reliability, high safety, and low cost [2,3]. According to different charge storage mechanisms, supercapacitors can be clarified into electrical double-layer capacitors (EDLCs) and pseudocapacitors. EDLCs are well-known for high specific power and long life span, whereas their specific energy is low due to limited charge storage of EDLC electrodes. Unlike EDLCs, pseudocapacitors store charges *via* the combination of capacitor-type surface/near-surface process and battery-type Faradic redox reaction, as a result, pseudocapacitors balance the contradiction between power and energy [4].

In recent years, great research efforts have been dedicated to exploring pseudocapacitive materials with suitable working potential and high specific capacitance. These materials include transitional metal oxides (RuO_2, MnO_2, Fe_2O_3, Co_3O_4, $CoMoO_4$, *etc.*) [5–8], hydroxides ($Ni(OH)_2$, $Cu(OH)_2$, layered double hydroxides, *etc.*) [9–11], sulfides ($NiCo_2S_4$, Ni_3S_2, MoS_2, *etc.*) [12–14], and conducting polymers (polyaniline (PANI) [15], polypyrrole (PPy) [16], polythiophene [17], *etc.*). Among them, MnO_2 has attracted considerable research interest, thanks to its high theoretical capacitance (1370 F g^{-1}), natural abundance, low cost, multiple valences, and environmental friendliness [18,19]. However, MnO_2 suffers from poor electrical conductivity (10^{-5} to 10^{-6} S m^{-1}) [20], which makes its experimental specific capacitance linger on a low level (100 to 300 F g^{-1}) for a long time [18]. In order to improve the pseudocapacitive kinetics of MnO_2, researchers use the following two strategies. The first strategy is to construct nanostructures, so as to increase the specific surface area accessible to the electrolyte and shorten diffusion lengths for both electrons and electrolyte ions. In this respect, MnO_2 nanoparticles [21], nanorods [22], nanowires [23], nanoflowers [24], nanotubes [25], nanobelts [26], nanosheets [27], and nanomeshs [28] have been reported with improved pseudocapacitive performances. Another strategy is to hybrid MnO_2 with highly conductive matrixes, such as

* Corresponding author.
E-mail addresses: chenjizhang@njfu.edu.cn, jizhang.chen@hotmail.com (J. Chen).

https://doi.org/10.1016/j.apsusc.2018.01.224
0169-4332/

conducting carbonaceous materials (*e.g.*, graphene [29–31], carbon nanotubes (CNT) [32], porous carbon [33]) and conductive polymers (*e.g.*, PANI [34], PPy [35], polythiophene [36]). As such, electrons are able to transport through these matrixes at a high rate, greatly lowering electrochemical polarization.

Nowadays, it is a hot topic to effectively utilize biomass resources, since huge amounts of them are harvested every year. In developing countries such as china, most of biomass resources end with agricultural wastes, which are usually burnt into air directly, aggravating the problem of air pollution. Actually, the intrinsic structure of biomass renders it an ideal precursor for producing porous carbon. In recent years, various biomass resources such as hemp, corn stalk, corn husk, rice husk, citrus peels, peanut shell, wheat straw, and cotton stalk have been reported as the carbon sources for EES applications [37,38]. In the present study, we propose to combine nanostructured birnessite-type MnO_2 with porous carbon derived from soybean stalk. Encouragingly, the product shows high specific capacitance, great rate capability, and superior cyclability, owing to the enhanced pseudocapacitive kinetics. Besides, an ASC device is constructed by using the biomass-derived porous carbon (BPC)/MnO_2 nanocomposite as the cathode material and FeS_2 nanobelts (denoted as N-FeS_2) as the anode material. The ASC is able to deliver high energy and power densities.

2. Experimental section

2.1. Materials synthesis

Soybean stalk was grown in Jiangsu Province (Eastern China), washed with de-ionized (DI) water, cut into pieces, and then dried overnight before use. The soybean stalk pieces were immersed in 6 M KOH aqueous solution for 8 h, filtered out without washing, and then dried at 80 °C in an oven. Subsequently, the soybean stalk pieces were annealed at 800 °C for 2 h under Ar atmosphere. After washed by 2 M HCl aqueous solution and DI water, and dried at 80 °C, biomass-derived porous carbon (BPC) was obtained. For the synthesis of BPC/MnO_2, 60 mL aqueous solution containing 60 mg BPC and 1.6 mmoL $KMnO_4$ was transferred into a 100 mL Teflon-lined stainless steel autoclave, and kept at 140 °C for 2 h. The BPC/MnO_2 was obtained after centrifugation, washing with DI water and ethanol, and drying at 80 °C overnight. For comparison, neat MnO_2 (N-MnO_2) was also fabricated by a hydrothermal reaction without the addition of BPC and with the reaction time increased to 20 h.

2.2. Characterization

The morphology and microstructure were characterized on a field emission scanning electron microscope (FE-SEM, NOVA Nano-SEM 230, FEI) and transmission electron microscope (TEM, JEM-2100F, JEOL) equipped with an energy dispersive X-ray spectroscopy (EDX) detector. The electrical conductivity was measured on a RTS-8 four-probe conductivity meter (Guangzhou, China). Powder X-ray diffraction (XRD) patterns were collected using a Da Vinci D8 ADVANCE diffractometer with Cu Kα radiation source (λ = 0.1540598 nm). Thermogravimetric analysis (TGA) was conducted on a Q5000 IR thermogravimetric analyzer (TA Instruments) at a heating rate of 10 °C min^{-1} under air atmosphere. Raman spectra were recorded from a Thermo Scientific DXR Raman Spectrometer under λ = 532 nm laser excitation. The surface chemical states were investigated by an X-ray photoelectron spectroscopy (XPS, ESCALAB 250Xi, Thermo Scientific). The N_2 adsorption/desorption measurements were carried out using a Quantachrome Autosorb-iQ2-MP analyzer.

2.3. Electrochemical measurements

To make working electrodes, a mixture of the active material, carbon black (Super-P), and polyvinylidene difluoride (PVDF) at a weight ratio of 8:1:1 was dispersed in N-methylpyrrolidone (NMP) to form a slurry, which was pasted onto nickel foams, air-dried at 80 °C for 1 h, and then dried at 110 °C under vacuum overnight. Electrochemical characterizations, including cyclic voltammetry (CV), galvanostatic charging/discharging (GCD), and electrochemical impedance spectroscopy (EIS), were performed on a CHI 660E electrochemical workstation in 1.0 M Na_2SO_4 aqueous electrolyte. The three-electrode configuration consisted of the working electrode, Pt plate (as the counter electrode), and Ag/AgCl (saturated KCl) reference electrode. CV and GCD tests were conducted based on the total mass of BPC and MnO_2. EIS measurements were carried out with the frequency ranging from 10 mHz to 100 kHz and the amplitude being set at 5 mV. ASCs were assembled by using BPC/MnO_2, N-FeS_2, and 1.0 M Na_2SO_4 aqueous solution as the positive electrode material, negative electrode material, and electrolyte, respectively. The synthesis process of N-FeS_2 can be found in our previous report [39]. Prior to the ASC assembly, the mass ratio of BPC/MnO_2 to N-FeS_2 was balanced according to: $q_+ = q_-$. CV and GCD tests were carried out on the basis of the total mass of BPC/MnO_2 and N-FeS_2.

3. Results and discussion

Fig. 1 shows the schematic for fabricating BPC/MnO_2. In step I, soybean stalk as the carbon source was converted to BPC *via* chemical activation. Soybean stalk is mainly composed of cellulose, hemicelluloses, and lignin. During the annealing process at 800 °C, KOH would be melt and etch carbonaceous materials. The etching rate of non-crystalline components (hemicelluloses and lignin) would be much faster than that of the crystalline cellulose, as a result, BPC is the carbonized product of cellulosic microfibrils. Therefore, BPC inherits the interconnected macroporous morphology from cellulose (see SEM images of BPC in Fig. 2a–c). According to four-probe method, BPC has a high electrical conductivity of 171 S m^{-1}. Although the electrical conductivity of BPC is not as high as that of graphite, carbon black, graphene, and multiwalled CNT, it is 100-fold higher than that of graphene foam [34,40]. Such high electrical conductivity renders BPC an ideal conductive matrix. Then in step II, nanostructured MnO_2 was grown on the BPC surface through hydrothermal reaction. Even at room temperature, $KMnO_4$ can react with carbonaceous materials as follows.

$$4MnO_4^- + 3C + H_2O \rightarrow 4MnO_2 + CO_3^{2-} + 2HCO_3^- \quad (1)$$

This redox reaction led to the coating of BPC by MnO_2 nanocrystals, which then functioned as the nucleation sites for the decomposition of $KMnO_4$ during hydrothermal process.

$$4MnO_4^- + 2H_2O \rightarrow 4MnO_2 + 4OH^- + 3O_2 \quad (2)$$

After the hydrothermal reaction, $KMnO_4$ can be decomposed completely, producing BPC/MnO_2 nanocomposite. Specific details of the fabrication process are provided in the Experimental section. The electrical conductivity of BPC/MnO_2 is 10.2 S m^{-1}. For comparison, N-MnO_2 was also prepared by hydrothermal reaction without the addition of BPC. From SEM images in Fig. 2d–f, we can see that N-MnO_2 is comprised by microspheres assembled by nanosheets.

The morphology and microstructure of BPC/MnO_2 were characterized by SEM and TEM, as show in Fig. 1b–f. It can be seen that MnO_2 is densely and uniformly dispersed on the surface of BPC, and it adopts two different morphologies, *i.e.*, nanosheets and nanowires. Specifically, most of MnO_2 exists in the form of thin nanosheets and aligns nearly vertically. Such morphology is in

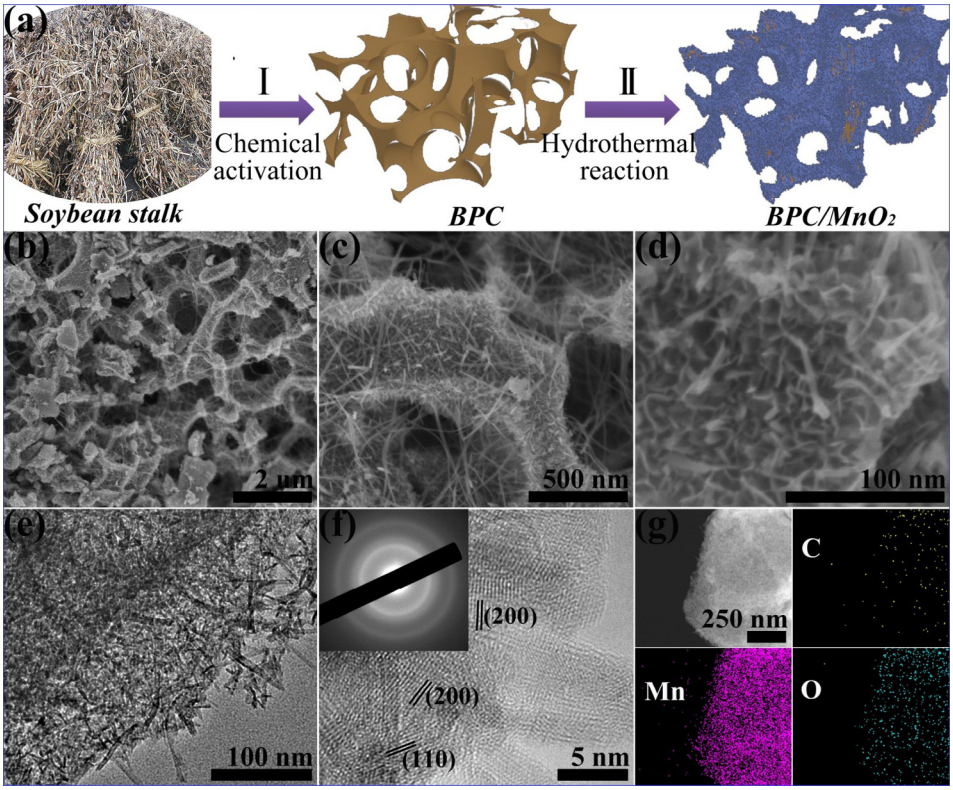

Fig. 1. (a) Schematic fabrication process, (b, c, d) SEM images, (e, f) TEM images, and (g) EDX mapping images of BPC/MnO_2.

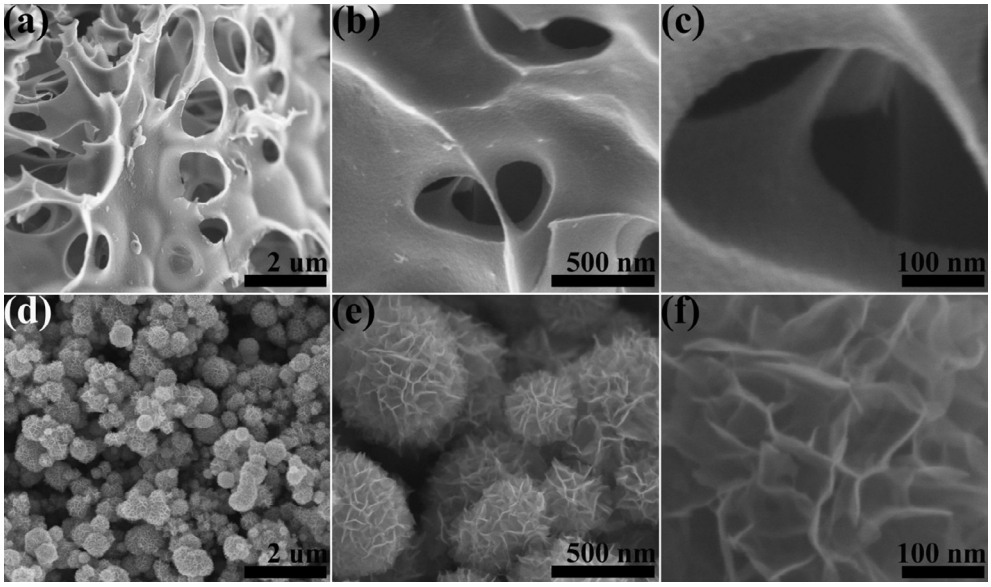

Fig. 2. SEM images of (a, b, c) BPC and (d, e, f) N-MnO_2.

favor of the penetration of electrolyte ions and exposure of active sites. The high-resolution TEM (HRTEM) image of BPC/MnO_2 is presented in Fig. 1f, revealing (2 0 0) and (1 1 0) planes of birnessite-type MnO_2. In addition, most of the lattice fringes are distorted, indicating low crystallinity of MnO_2, which is further confirmed by the selected area electron diffraction (SAED) pattern in the inset of Fig. 1f. Fig. 1 g shows EDX mapping results of BPC/MnO_2. The C, Mn, and O elements are observed to overlap with the STEM image, demonstrating MnO_2 is uniformly grown on the BPC matrix.

The crystal structures of the three products were investigated by XRD measurements, as shown in Fig. 3a. BPC displays a broad diffraction peak centered at around 24°, associating with the (002) plan of pseudographitic phase. The broadness of this peak indicates low graphitization degree, which results from the low

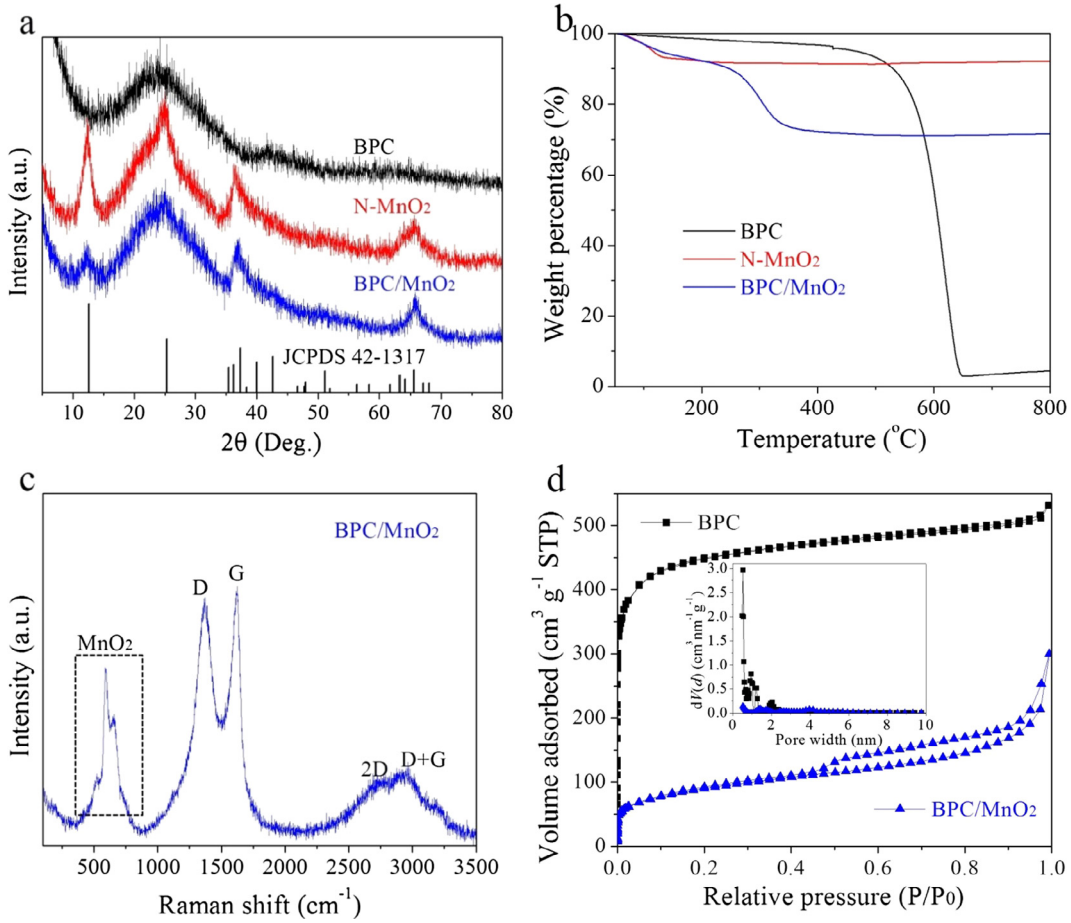

Fig. 3. (a) XRD patterns and (b) TGA curves of BPC, N-MnO_2, and BPC/MnO_2. (c) Raman spectrum of BPC/MnO_2. (d) N_2 adsorption/desorption isotherms of BPC and BPC/MnO_2 (the inset shows corresponding NLDFT pore-size distributions).

carbonization temperature (800 °C). As for N-MnO_2, all the peaks can be indexed as birnessite-type MnO_2 (JCPDS 42-1317) with a lamellar structure. As is expected, the XRD pattern of BPC/MnO_2 is the combination of BPC and N-MnO_2. Besides, the broad peaks further verify low-crystalline characteristic of MnO_2 in this nanocomposite. TGA curves of the products were recorded in air atmosphere and are shown in Fig. 3b. The weight loss below 250 °C can be attributed to the desorption of surface-adsorbed water and the evaporation of water molecules bound in the birnessite lattice, while the weight loss above 250 °C is due to the consumption of carbon. It is also noted that the consumption of carbon in BPC/MnO_2 occurs at much lower temperature than that in BPC. This phenomenon is due to the catalyzing effect of MnO_2 on carbon consumption [41,42]. According to these three TG curves, the mass percentage of MnO_2 in BPC/MnO_2 is estimated to be 76.7%. Raman spectrum of BPC/MnO_2 is shown in Fig. 3c. Typically, two strong peaks located at around 1370 and 1620 cm^{-1} are assigned to the disorder-induced D band and sp^2 vibration G band (graphitic structure) of carbonaceous materials, respectively [43]. Besides, there exist two humps in the range from 2500 to 3200 cm^{-1}, relating with 2D and D + G bands of carbon. In the low wavenumber region, three peaks at around 520, 590, and 660 cm^{-1} are attributed to birnessite-type MnO_2 [44].

Fig. 3d shows N_2 adsorption/desorption isotherms of BPC and BPC/MnO_2. BPC exhibits type I isotherm (IUPAC classification) with high adsorption capacity, indicating BPC possesses abundant micropores. In contrast, BPC/MnO_2 presents type IV isotherm with a representative H4-type hysteresis loop, indicative of mesoporous structure. After MnO_2 is anchored onto BPC, it fills most of the micropores in BPC and generates mesopores. According to Bru nauer–Emmett–Teller (BET) analysis, the specific surface area of BPC and BPC/MnO_2 is 1709.5 and 325.1 $m^2 g^{-1}$, respectively. The pore-size distributions of BPC and BPC/MnO_2 on the basis of non-local density functional theory (NLDFT) model are shown in the inset of Fig. 3d, confirming the above speculations. For BPC/MnO_2, a peak centered at *ca.* 4.0 nm can be observed, which might originate from the voids among MnO_2 nanosheets. Besides, the pore volume of BPC and BPC/MnO_2 is found to be 0.779 and 0.337 $cm^3 g^{-1}$, respectively. Such rich porosity is beneficial for supercapacitor applications.

XPS technique was employed to acquire insight into surface chemical compositions and valence states of BPC/MnO_2. The survey XPS spectrum in Fig. 4a contains the signals of C, Mn, O, and K, according well with previous reported birnessite-type MnO_2 [33,45]. The deconvolution of the C1s high-resolution spectrum is shown in Fig. 4b. The most pronounced peaks is centered at 284.7 eV, which is characteristic of sp^2 graphitic lattice (C—C and C═C), while three other subpeaks at 286.5, 285.3, and 284.7 eV are associated with O—C═O, C═O, and C—O functional groups, respectively [46]. The high-resolution Mn 2p spectrum (Fig. 4c) exhibits two peaks at 642.6 and 654.1 eV, which can be ascribed to Mn $2p_{3/2}$ and Mn $2p_{1/2}$, respectively [47]. The spin-energy separation of 11.5 eV indicates that the oxidation state of Mn is primarily +4. In Fig. 4d, the high-resolution O 1s spectrum can be fitted

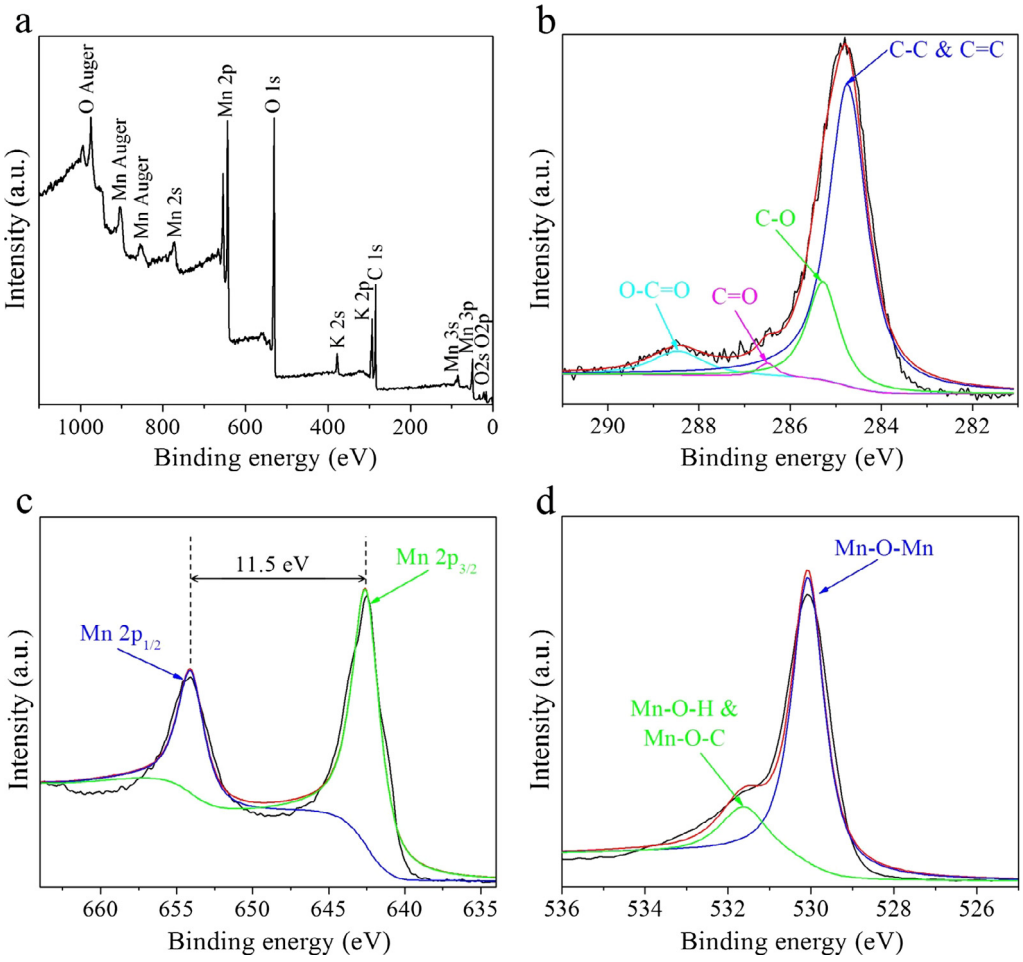

Fig. 4. (a) Survey, (b) high-resolution C 1s, (c) high-resolution Mn 2p, and (d) high-resolution O 1s XPS spectra of BPC/MnO_2.

into two components, *i.e.*, 530.1 eV (Mn—O—Mn) and 531.6 eV (Mn—O—H & Mn—O—H) [48].

The electrochemical performances of the products were explored with a three-electrode setup. The CV curves of BPC, N-MnO_2, and BPC/MnO_2 at various scan rates are shown in Fig. 5a–c. These CV curves exhibit quasi-rectangular shape at low scan rates, indicative of capacitor-like surface or near-surface charge storage mechanism. When the scan rate is increased to 100 mV s^{-1}, the quasi-rectangular shape can be well preserved, demonstrating low electrochemical polarization. Besides, tiny humps are observed for BPC/MnO_2, resulting from improved Mn^{4+}/Mn^{3+} redox reaction [49,50]. Based on the integral area of CV curves, the specific capacitances can be calculated according to the procedure described in Supporting Information. Obviously, BPC/MnO_2 possesses much higher capacitances than that of BPC and N-MnO_2 throughout all the scan rates, suggesting that the charge storage activity can be significantly improved after anchoring nanostructured MnO_2 onto BPC. In order to clarify the charge storage kinetics, we introduced a classic power-law equation $i = av^b$, where i and v represent the peak current and scan rate, respectively, and a and b are adjustable parameters [51]. This reaction can be transformed into $\lg(C^* v) = \lg(a) + b * \lg(v)$, where C represents the specific capacitance. It can be seen that the b value can be determined from the slope of $\lg(C^* v)$ *vs.* $\lg(v)$. In particular, the b value can be used to distinguish different charge storage mechanisms. If b approaches 0.5, the charge storage process is controlled by the bulk diffusion of electrolyte ions. Otherwise if b approaches 1.0, the charge storage is dominated by capacitor-like process, *i.e.*, surface ion adsorption, surface/near-surface redox reaction, or pseudocapacitive intercalation. We should also realize the b value cannot possibly reach 1 due to the inevitable impedances. As is seen in Fig. 5d, BPC has rather high b values, confirming that BPC is an appealing matrix for supporting pseudocapacitive materials. In the case of BPC/MnO_2, its b value is 0.859 from 5 to 50 mV s^{-1} and 0.677 from 50 to 100 mV s^{-1}, which is considerably higher than that of N-MnO_2, revealing enhanced pseudocapacitive kinetics after introducing BPC as the matrix.

The GCD curves of BPC, MnO_2, and BPC/MnO_2 were collected at various current densities, as shown in Fig. 6a–c. These curves are almost symmetric during charging and discharging processes, manifesting ideal capacitive behaviors. Fig. 6d summarizes specific capacitances calculated from the corresponding discharging curves. Although BPC gives excellent rate capability, its capacitance is lower than 200 F g^{-1}. As for BPC/MnO_2, it delivers high capacitance of 384.9 F g^{-1} at a current density of 0.5 A g^{-1}. When the current density is increased to 40-fold (20 A g^{-1}), 48.1% of the capacitance at 0.5 A g^{-1} can be maintained. In comparison, the specific capacitance of N-MnO_2 is 241.5 F g^{-1} at 0.5 A g^{-1}, whereas merely 18.6% can be retained at 20 A g^{-1}. These results indicate high specific capacitance and great rate capability of BPC/MnO_2 nanocomposite. Impressively, BPC/MnO_2 outperforms many recently reported MnO_2-based electrode materials, such as the ones listed in Table 1 [26,29,52–63].

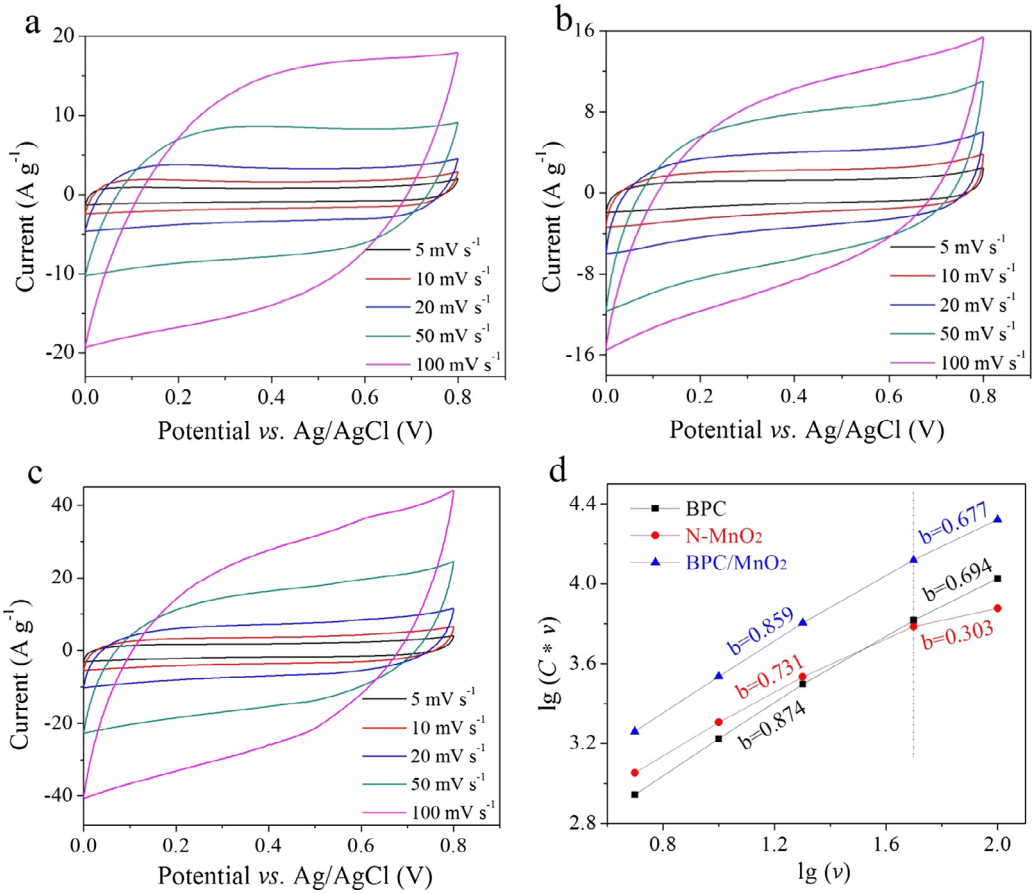

Fig. 5. CV curves of (a) BPC, (b) N-MnO_2, and (c) BPC/MnO_2 at scan rates from 5 to 100 mV s^{-1}. (d) Evolutions of the b value obtained from the power law equation for BPC, N-MnO_2, and BPC/MnO_2.

EIS measurements were also used to investigate the electrochemical properties of BPC, MnO_2, and BPC/MnO_2, as shown in Fig. 7a. All the products exhibit a small depressed semicircle in the high frequency region and nearly a straight line in the low frequency region. The EIS spectra were fitted using an equivalent circuit model in the inset of Fig. 7a. This circuit consists of six elements, namely bulk resistance R_s, pseudocapacitance C_{pseudo}, leakage resistance R_l in parallel with C_{pseudo}, EDLC capacitance C_{dl}, charge transfer resistance R_{ct}, and Warburg impedance (W). The fitted values of these elements are listed in Table 2. R_s includes contributions from the electrical resistance of the electrode, the ionic resistance of the electrolyte, and the contact resistance at the interface between active material and current collector. BPC and BPC/MnO_2 show low R_s values of around 1.0 Ω, which is slightly lower than 1.11 Ω of N-MnO_2. R_{ct} is an indicator of interface kinetics. BPC/MnO_2 has a lower R_{ct} (1.05 Ω) than that (1.60 Ω) of N-MnO_2, reflecting enhanced charge transfer kinetics when BPC is introduced as the conductive matrix.

Cyclability is another important factor for evaluating electrodes materials. Fig. 7b shows that BPC retains 96.0% of its initial capacitance after 5000 cycles, corroborating excellent durability as a supporting matrix. As for N-MnO_2, the repeated redox reactions would bring in volumetric and structural changes of MnO_2, leading to continuous capacitance fading during long-term cycles. As a result, N-MnO_2 can only maintain 73.3% of its initial capacitance after 5000 cycles. The introduction of BPC matrix can help buffer volumetric expansion and prevent structural breakdown of MnO_2, therefore contributing to high capacitance retention of BPC/MnO_2 (90.7% after 5000 cycles), which is comparable to that of recently reported MnO_2 (see Table 1). The great performances of BPC/MnO_2 discussed above can be ascribed to the following factors. Firstly, the ultrathin nanostructured morphology of MnO_2 can not only provide large active surface area but also facilitate charge transports. Secondly, BPC matrix acts as a highway for electrons, which greatly lowers electrochemical polarization and enhances pseudocapacitive kinetics. Thirdly, BPC can stabilize MnO_2 upon redox reactions. Fourthly, low-crystalline or amorphous phases are capable of achieving faster charge transports and better cycling stability than their high-crystalline counterparts, owing to their more structural defects and disorder [4,64].

Given that BPC/MnO_2 in the present work and N-FeS_2 in our previous work [39] possess stable and compatible potential windows of 0 to 0.8 V and −1.0 to 0 V in 1.0 M Na_2SO_4 aqueous electrolyte, respectively (Fig. 8a), it is expected that a 1.8 V ASC can be constructed by integrating these two electrode materials. To balance charges in these two electrodes, the mass ratio of BPC/MnO_2 to N-FeS_2 is set as 1–1.1: 1. The CV curve of the ASC in Fig. 8a shows quasi-rectangular shape, indicative of pseudocapacitive charge storage mechanism. The Nyquist plots of the ASC in Fig. 8b reveal low impedances (*e.g.*, R_{ct} = 2.11 Ω), demonstrating fast charge transports. GCD curves of the ASC at different current densities are shown in Fig. 8c. The specific capacitance of the ASC (based on the total mass of two electrode materials, see calculation procedure in Supporting

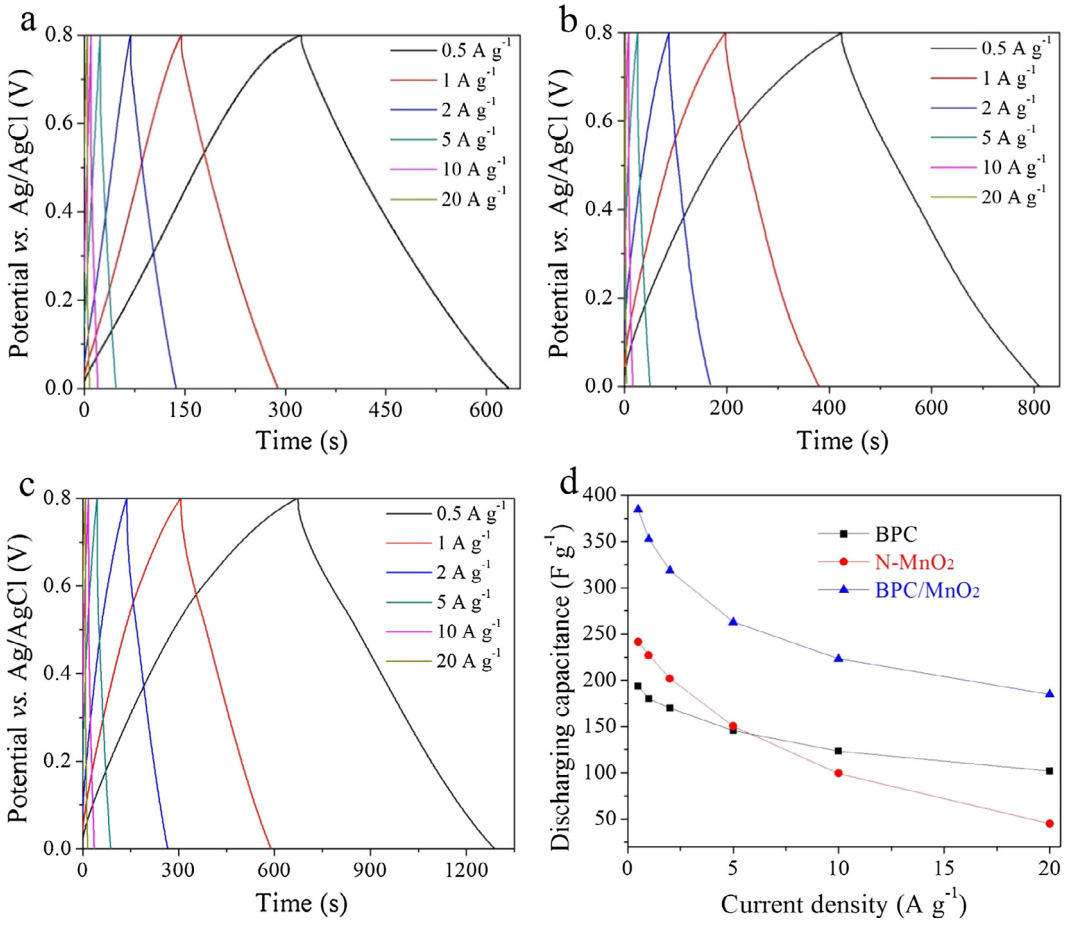

Fig. 6. GCD curves of (a) BPC, (b) N-MnO_2, and (c) BPC/MnO_2 at current densities from 0.5 to 20 A g^{-1}. (d) Comparative specific capacitances of BPC, N-MnO_2, and BPC/MnO_2 at different current densities.

Table 1
Comparison of the specific capacitance and cyclability of BPC/MnO_2 nanocomposite in this report with other MnO_2-based electrode materials reported in recent three years.

Electrode material	Electrolyte	Specific capacitance	Cyclability	Ref. (Year)
BPC/MnO_2 nanocomposite	1 M Na_2SO_4	384.9 F g^{-1} at 0.5 A g^{-1}	90.7% after 5000 cycles	This report
	1 M Na_2SO_4	352.8 F g^{-1} at 1.0 A g^{-1}		
Graphene/MnO_2 nanoflowers	0.5 M Li_2SO_4	240 F g^{-1} at 1 A g^{-1}	96% after 1000 cycles	[52] (2015)
Graphene/C/MnO_2 nanospheres	1 M Na_2SO_4	255 F g^{-1} at 0.5 A g^{-1}	83% after 1000 cycles	[29] (2015)
Melosira-type MnO_2 pattern	1 M Na_2SO_4	371.2 F g^{-1} at 0.5 A g^{-1}	93.1% after 2000 cycles	[53] (2015)
MnO_2 nanobelts	1 M Na_2SO_4	278 F g^{-1} at 0.2 A g^{-1}	91.3% after 1000 cycles	[26] (2016)
CNT/MnO_2 hybrid film	1 M Na_2SO_4	300 F g^{-1} at 0.1 A g^{-1}	75% after 1600 cycles	[54] (2016)
Fe-doped nano-MnO_2	1 M Na_2SO_4	267.0 F g^{-1} at 0.1 A g^{-1}	100% after 2000 cycles	[55] (2016)
Mesoporous α-MnO_2	1 M Na_2SO_4	322 F g^{-1} at 1 A g^{-1}	90% after 8000 cycles	[56] (2016)
α-MnO_2 NWs@δ-MnO_2 NSs	6 M KOH	310.2 F g^{-1} at 0.5 A g^{-1}	98% after 10,000 cycles	[57] (2016)
CuO@MnO_2 nanostructures	1 M Na_2SO_4	344 F g^{-1} at 0.25 A g^{-1}	83% after 12,000 cycles	[58] (2016)
MnO_2@graphdiyne oxides	1 M Na_2SO_4	301 F g^{-1} at 0.2 A g^{-1}	98% after 3000 cycles	[59] (2017)
PPy/mesoporous MnO_2	1 M Na_2SO_4	320 F g^{-1} at 0.5 A g^{-1}	91.4% after 5000 cycles	[60] (2017)
Graphene/MnO_2 nanoparticle	1 M Na_2SO_4	324 F g^{-1} at 0.4 A g^{-1}	91.1% after 5000 cycles	[61] (2017)
Starfish-like MnO_2 nanosheets	1 M Na_2SO_4	336 F g^{-1} at 1 A g^{-1}	125% after 7000 cycles	[62] (2017)
Graphene/flower-like MnO_2	1 M Na_2SO_4	220 F g^{-1} at 0.5 A g^{-1}	98.3% after 1000 cycles	[63] (2018)

Information) is 80.3 F g^{-1} at 0.5 A g^{-1}, and remains 30.5 F g^{-1} when the current density is increased to 15 A g^{-1}. Given that specific energy and specific power are two crucial factors for practical applications, we provide Ragone plots of our ASC device in Fig. 8d. The maximum specific energy is 34.2 Wh kg^{-1} at 425 W kg^{-1}, while the maximum specific power is 9.58 kW kg^{-1} at 9.73 Wh kg^{-1}. Such performance rivals many MnO_2-based ASCs, such as the ones plotted in Fig. 8d [33,50,58,65,66]. To demonstrate the practicability of our ASC configuration, we used two ASCs connected in series to power three LEDs, as shown in the inset of Fig. 8d and Supplementary Video.

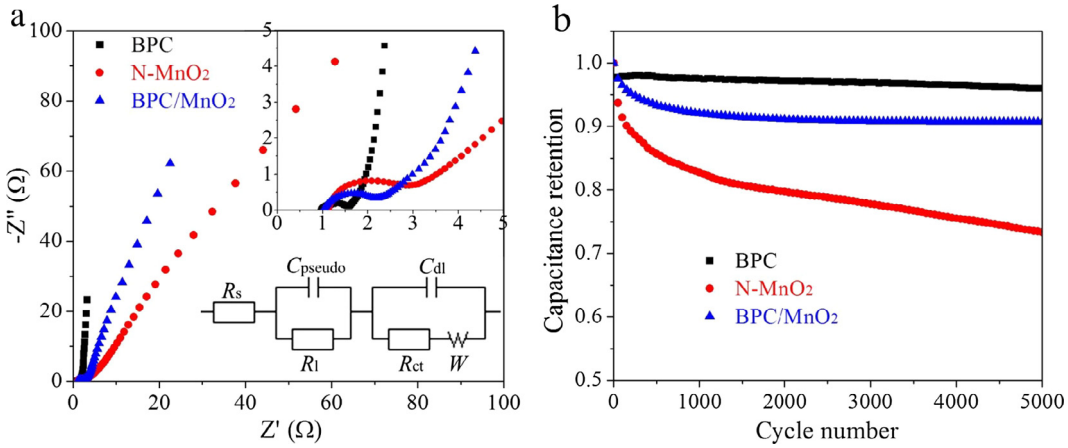

Fig. 7. (a) Nyquist plots and (b) cycling performances of BPC, N-MnO_2, and BPC/MnO_2.

Table 2
Fitted values of different elements based on the corresponding Nyquist plots in Fig. 7a.

Product	R_s (Ω)	R_{ct} (Ω)	R_l (Ω)	C_{dl} (mF)	C_{psudo} (mF)	W (Ω $s^{-0.5}$)
BPC	0.97	0.430	0.836	498	1.79	38.2
N-MnO_2	1.11	1.60	130	0.212	256	8.07
BPC/MnO_2	1.02	1.05	296	0.351	294	3.00

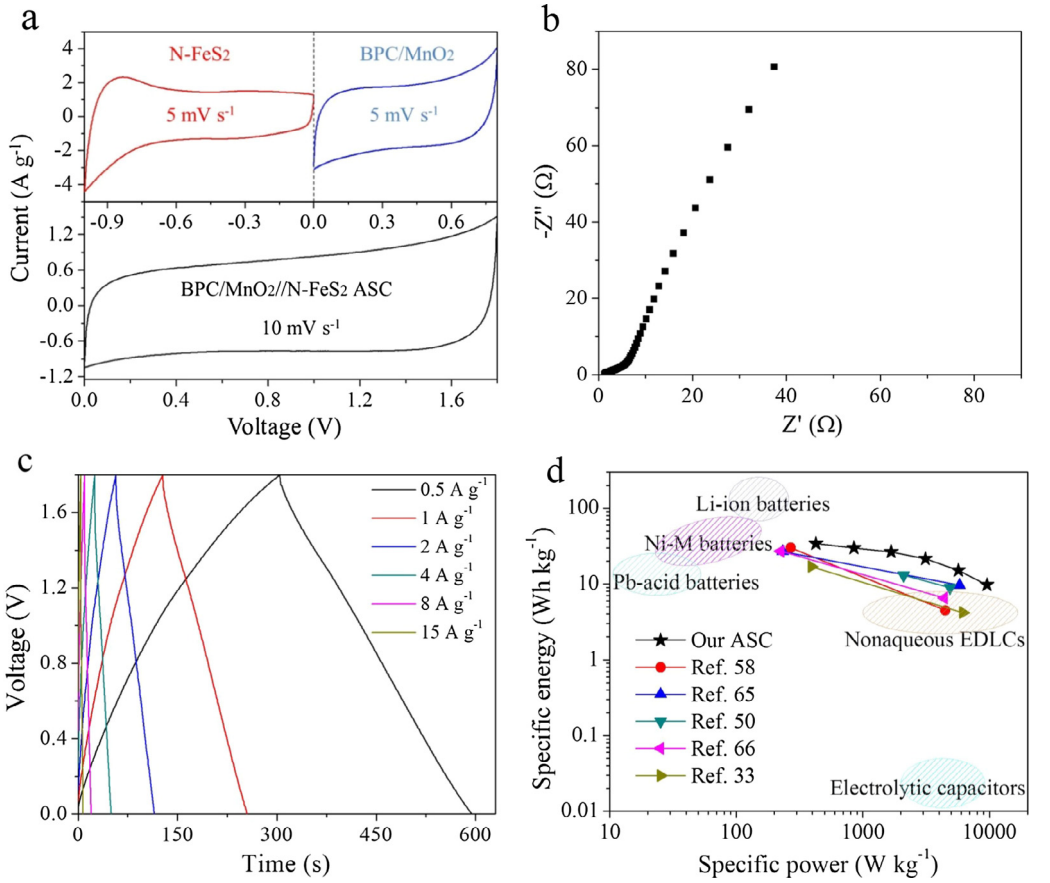

Fig. 8. (a) CV curves of the negative electrode material N-FeS_2, positive electrode material BPC/MnO_2, and BPC/MnO_2//N-FeS_2 ASC. (b) Nyquist plots of the ASC. (c) GCD curves of the ASC at different current densities. (d) Ragone plots of our ASC *vs.* recently reported MnO_2-based ASCs. The inset of d demonstrates two ASCs connected in series to power three LEDs.

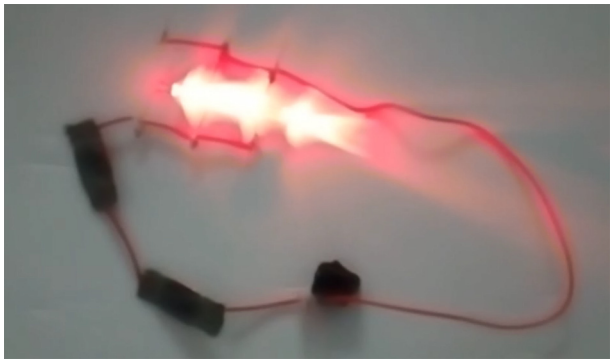

Supplementary Video

4. Conclusion

In summary, a nanocomposite consisting of soybean stalk-derived porous carbon and low-crystalline nanostructured MnO_2 is fabricated by a high-temperature activation process and subsequent hydrothermal reaction. The intriguing heterostructured nanoarchitecture, featuring highly conductive porous matrix, large surface area, and short ion/electron transport paths, endows BPC/MnO_2 with enhanced pseudocapacitive kinetics. This nanocomposite delivers high specific capacitances of 384.9 and 185.0 F g^{-1} at current densities of 0.5 and 20 A g^{-1}, respectively, and retains 90.7% of its initial capacitance after 5000 cycles. In addition, an ASC device made of BPC/MnO_2 cathode and N-FeS_2 anode achieves high specific energy of 34.2 Wh kg^{-1} and high specific power of 9.58 kW kg^{-1}. In this work, the demonstration of anchoring nanostructured metal oxide onto biomass-derived porous carbon offers a good strategy to realize efficient, reliable, and cost-effective energy storage.

Acknowledgements

This work was supported by the Natural Science Foundation of Jiangsu Province (BK20170917), the Scientific Research Foundation for High-Level Talents of Nanjing Forestry University (GXL2016023), the Training Program of Innovation and Entrepreneurship for Undergraduates of Jiangsu Province (201710298018Z), and the Research Grants Council of Hong Kong (Theme-based Research Scheme, T23-407/13-N).

Appendix A. Supplementary material

Supplementary data associated with this article can be found, in the online version, at https://doi.org/10.1016/j.apsusc.2018.01.224.

References

[1] M.R. Palacin, A. de Guibert, Science 351 (2016) 1253292.
[2] P. Huang, C. Lethien, S. Pinaud, K. Brousse, R. Laloo, V. Turq, M. Respaud, A. Demortiere, B. Daffos, P.L. Taberna, B. Chaudret, Y. Gogotsi, P. Simon, Science 351 (2016) 691–695.
[3] H.S. Kim, J.B. Cook, H. Lin, J.S. Ko, S.H. Tolbert, V. Ozolins, B. Dunn, Nat. Mater. 16 (2017) 454–460.
[4] K.A. Owusu, L. Qu, J. Li, Z. Wang, K. Zhao, C. Yang, K.M. Hercule, C. Lin, C. Shi, Q. Wei, L. Zhou, L. Mai, Nat. Commun. 8 (2017) 14264.
[5] P. Yang, Y. Ding, Z. Lin, Z. Chen, Y. Li, P. Qiang, M. Ebrahimi, W. Mai, C.P. Wong, Z.L. Wang, Nano Lett. 14 (2014) 731–736.
[6] C. Zhang, T.M. Higgins, S.-H. Park, S.E. O'Brien, D. Long, J.N. Coleman, V. Nicolosi, Nano Energy 28 (2016) 495–505.
[7] Y. Jiang, L. Chen, H. Zhang, Q. Zhang, W. Chen, J. Zhu, D. Song, Chem. Eng. J. 292 (2016) 1–12.
[8] J. Wang, X. Zhang, Q. Wei, H. Lv, Y. Tian, Z. Tong, X. Liu, J. Hao, H. Qu, J. Zhao, Y. Li, L. Mai, Nano Energy 19 (2016) 222–233.
[9] X. Zhang, J. Xiao, X. Zhang, Y. Meng, D. Xiao, Electrochim. Acta 191 (2016) 758–766.
[10] A.D. Jagadale, G. Guan, X. Li, X. Du, X. Ma, X. Hao, A. Abudula, J. Power Sources 306 (2016) 526–534.
[11] J. Chen, J. Xu, S. Zhou, N. Zhao, C.-P. Wong, J. Mater. Chem. A 3 (2015) 17385–17391.
[12] R. Li, S. Wang, J. Wang, Z. Huang, PCCP 17 (2015) 16434–16442.
[13] H. Wang, H. Feng, J. Li, Small 10 (2014) 2165–2181.
[14] H. Fan, W. Liu, W. Shen, Chem. Eng. J. 326 (2017) 518–527.
[15] D. Ge, L. Yang, L. Fan, C. Zhang, X. Xiao, Y. Gogotsi, S. Yang, Nano Energy 11 (2015) 568–578.
[16] W.K. Chee, H.N. Lim, I. Harrison, K.F. Chong, Z. Zainal, C.H. Ng, N.M. Huang, Electrochim. Acta 157 (2015) 88–94.
[17] A. Alabadi, S. Razzaque, Z. Dong, W. Wang, B. Tan, J. Power Sources 306 (2016) 241–247.
[18] W. Wei, X. Cui, W. Chen, D.G. Ivey, Chem. Soc. Rev. 40 (2011) 1697–1721.
[19] M.A. Borysiewicz, M. Ekielski, Z. Ogorzalek, M. Wzorek, J. Kaczmarski, T. Wojciechowski, Nanoscale 9 (2017) 7577–7587.
[20] G.H. Yu, L.B. Hu, N.A. Liu, H.L. Wang, M. Vosgueritchian, Y. Yang, Y. Cui, Z.A. Bao, Nano Lett. 11 (2011) 4438–4442.
[21] X.H. Li, G.Y. Wang, X.W. Wang, X.P. Li, J.H. Ji, J. Mater. Chem. A 1 (2013) 10103–10106.
[22] X.L. Wang, A.B. Yuan, Y.Q. Wang, J. Power Sources 172 (2007) 1007–1011.
[23] J. Song, H. Li, S. Li, H. Zhu, Y. Ge, S. Wang, X. Feng, Y. Liu, New J. Chem. 41 (2017) 3750–3757.
[24] J.P. Ni, W.C. Lu, L.M. Zhang, B.H. Yue, X.F. Shang, Y. Lv, J. Phys. Chem. C 113 (2009) 54–60.
[25] J.X. Zhu, W.H. Shi, N. Xiao, X.H. Rui, H.T. Tan, X.H. Lu, H.H. Hng, J. Ma, Q.Y. Yan, ACS Appl. Mater. Interf. 4 (2012) 2769–2774.
[26] M. Aghazadeh, M.G. Maragheh, M.R. Ganjali, P. Norouzi, F. Faridbod, Appl. Surf. Sci. 364 (2016) 141–147.
[27] M. Kundu, L. Liu, J. Power Sources 243 (2013) 676–681.
[28] Z. Wang, F. Wang, J. Mater. Chem. A 5 (2017) 9709–9716.
[29] Y. Xiong, M. Zhou, H. Chen, L. Feng, Z. Wang, X. Yan, S. Guan, Appl. Surf. Sci. 357 (2015) 1024–1030.
[30] Y. Liu, X. Miao, J. Fang, X. Zhang, S. Chen, W. Li, W. Feng, Y. Chen, W. Wang, Y. Zhang, ACS Appl. Mater. Interf. 8 (2016) 5251–5260.
[31] K. Hareesh, B. Shateesh, R.P. Joshi, J.F. Williams, D.M. Phase, S.K. Haram, S.D. Dhole, RSC Adv. 7 (2017) 20027–20036.
[32] Y. Li, Int. J. Electrochem. Sci. 12 (2017) 4733–4744.
[33] T. Liu, C. Jiang, W. You, J. Yu, J. Mater. Chem. A 5 (2017) 8635–8643.
[34] K. Ghosh, C.Y. Yue, M.M. Sk, R.K. Jena, ACS Appl. Mater. Interf. 9 (2017) 15350–15363.
[35] W. Yao, H. Zhou, Y. Lu, J. Power Sources 241 (2013) 359–366.
[36] R. Liu, S.B. Lee, J. Am. Chem. Soc. 130 (2008) 2942–2943.
[37] W. Tang, Y. Zhang, Y. Zhong, T. Shen, X. Wang, X. Xia, J. Tu, Mater. Res. Bull. 88 (2017) 234–241.
[38] J. Chen, X. Zhou, C. Mei, J. Xu, S. Zhou, C.-P. Wong, J. Power Sources 342 (2017) 48–55.
[39] J. Chen, X. Zhou, C. Mei, J. Xu, S. Zhou, C.-P. Wong, Electrochim. Acta 222 (2016) 172–176.
[40] B. Marinho, M. Ghislandi, E. Tkalya, C.E. Koning, G. de With, Powder Technol. 221 (2012) 351–358.
[41] Y. Peng, Z. Chen, J. Wen, Q. Xiao, D. Weng, S. He, H. Geng, Y. Lu, Nano Res. 4 (2010) 216–225.
[42] B. Shen, Qinlei, Energy Convers. Manage. 47 (2006) 1429–1437.
[43] J.R. Miller, R.A. Outlaw, B.C. Holloway, Science 329 (2010) 1637–1639.
[44] A. Ogata, S. Komaba, R. Baddour-Hadjean, J.P. Pereira-Ramos, N. Kumagai, Electrochim. Acta 53 (2008) 3084–3093.
[45] J. Yan, Z. Fan, T. Wei, W. Qian, M. Zhang, F. Wei, Carbon 48 (2010) 3825–3833.
[46] G. Zhu, C. Xi, Y. Liu, J. Zhu, X. Shen, J. Mater. Chem. A 3 (2015) 7591–7599.
[47] P.-Y. Kuang, M.-H. Liang, W.-Y. Kong, Z.-Q. Liu, Y.-P. Guo, H.-J. Wang, N. Li, Y.-Z. Su, S. Chen, New J. Chem. 39 (2015) 2497–2505.
[48] D. Yan, P.X. Yan, S. Cheng, J.T. Chen, R.F. Zhuo, J.J. Feng, G.A. Zhang, Cryst. Growth Des. 9 (2009) 218–222.
[49] N.R. Chodankar, D.P. Dubal, G.S. Gund, C.D. Lokhande, Electrochim. Acta 165 (2015) 338–347.
[50] D. Gueon, J.H. Moon, A.C.S. Sustain, Chem. Eng. 5 (2017) 2445–2453.
[51] V. Augustyn, J. Come, M.A. Lowe, J.W. Kim, P.L. Taberna, S.H. Tolbert, H.D. Abruna, P. Simon, B. Dunn, Nat. Mater. 12 (2013) 518–522.
[52] J. Liu, Y. Zhang, Y. Li, J. Li, Z. Chen, H. Feng, J. Li, J. Jiang, D. Qian, Electrochim. Acta 173 (2015) 148–155.
[53] F. Li, Y. Xing, M. Huang, K.L. Li, T.T. Yu, Y.X. Zhang, D. Losic, J. Mater. Chem. A 3 (2015) 7855–7861.
[54] H. Chen, S. Zeng, M. Chen, Y. Zhang, L. Zheng, Q. Li, Small 12 (2016) 2035–2045.
[55] Z. Wang, F. Wang, Y. Li, J. Hu, Y. Lu, M. Xu, Nanoscale 8 (2016) 7309–7317.
[56] S. Bag, C.R. Raj, J. Mater. Chem. A 4 (2016) 587–595.
[57] Z. Ma, G. Shao, Y. Fan, G. Wang, J. Song, D. Shen, ACS Appl. Mater. Interf. 8 (2016) 9050–9058.
[58] H. Chen, M. Zhou, T. Wang, F. Li, Y.X. Zhang, J. Mater. Chem. A 4 (2016) 10786–10793.
[59] J. Xu, J. Li, Q. Yang, Y. Xiong, C. Chen, Electrochim. Acta 251 (2017) 672–680.
[60] N. Wang, P. Zhao, K. Liang, M. Yao, Y. Yang, W. Hu, Chem. Eng. J. 307 (2017) 105–112.
[61] P. Wang, C. Zhou, S. Wang, H. Kong, Y. Li, S. Li, S. Sun, J. Mater. Sci.-Mater. El. 28 (2017) 12514–12522.

[62] B. Xu, L. Yu, M. Sun, F. Ye, Y. Zhong, G. Cheng, H. Wang, Y. Mai, RSC Adv. 7 (2017) 14910–14916.
[63] J. Dong, G. Lu, F. Wu, C. Xu, X. Kang, Z. Cheng, Appl. Surf. Sci. 427 (2018) 986–993.
[64] J. Chen, J. Xu, S. Zhou, N. Zhao, C.-P. Wong, Nano Energy 21 (2016) 145–153.
[65] Y. Saito, M. Meguro, M. Ashizawa, K. Waki, R. Yuksel, H.E. Unalan, H. Matsumoto, RSC Adv. 7 (2017) 12351–12358.
[66] A.V. Radhamani, K.M. Shareef, M.S. Rao, ACS Appl. Mater. Interf. 8 (2016) 30531–30542.